

Published in final edited form as:

Neuroimage. 2010 January 1; 49(1): 561–567. doi:10.1016/j.neuroimage.2009.07.033.

Anatomical Atlas-Guided Diffuse Optical Tomography of Brain Activation

Anna Custo^{a,b,*}, David A. Boas^b, Daisuke Tsuzuki^c, Ippeita Dan^c, Rickson Mesquita^{b,d}, Bruce Fischl^{a,b}, W. Eric L. Grimson^a, and Williams Wells, III^{a,e}

^aMassachusetts Institute of Technology, Computer Science and Artificial Intelligence Laboratory, Cambridge, MA, 02139, USA

^bAthinoula A. Martinos Center for Biomedical Imaging, Massachusetts General Hospital, Harvard Medical School, Charlestown, MA, USA

^cNational Food Research Institute, 2-1-12 Kannondai, Tsukuba 305-8642, Japan

^dInstitute of Physics, University of Campinas, Campinas, SP, 13083-970, Brazil

^eHarvard Medical School, Brigham Women's Hospital, Boston, MA, 02115, USA

Abstract

We describe a neuro imaging protocol that utilizes an anatomical atlas of the human head to guide Diffuse optical tomography of human brain activation. The protocol is demonstrated by imaging the hemodynamic response to median nerve stimulation in three healthy subjects, and comparing the images obtained using a head atlas with the images obtained using the subject-specific head anatomy. The results indicate that using the head atlas anatomy it is possible to reconstruct the location of the brain activation to the expected gyrus of the brain, in agreement with the results obtained with the subject-specific head anatomy. The benefits of this novel method derive from eliminating the need for subject-specific head anatomy and thus obviating the need for a subject-specific MRI to improve the anatomical interpretation of Diffuse optical tomography images of brain activation.

Keywords

Diffuse Optical Tomography; NIRS; anatomical atlas; MRI; segmentation; registration; inverse problem; human study; somatosensory; *PACS*: 87.19.lf; *PACS*: 87.19.lh

Introduction

Diffuse Optical Tomography (DOT) is the tomographic variant of Near Infrared Spectroscopy (NIRS). These methods complement functional Magnetic Resonance Imaging (fMRI) of human brain activation by providing measures of changes in both oxygenated (HbO) and deoxygenated (HbR) hemoglobin with a superior temporal resolution (see Obrig

© 2009 Elsevier Inc. All rights reserved.

* Corresponding author custo@csail.mit.edu (Anna Custo).

¹Via Murcarolo 6/10, 16167, Genova (GE), Italy (+39 347 2104445)

Publisher's Disclaimer: This is a PDF file of an unedited manuscript that has been accepted for publication. As a service to our customers we are providing this early version of the manuscript. The manuscript will undergo copyediting, typesetting, and review of the resulting proof before it is published in its final citable form. Please note that during the production process errors may be discovered which could affect the content, and all legal disclaimers that apply to the journal pertain.

and Villringer (2003); Strangman et al. (2002); Shibasaki (2008); Toronov et al. (2007) for a review). NIRS requires only compact experimental systems, is less restrictive, and is relatively forgiving of body movement, and thus provides one with a wide variety of flexible measurement options of brain function in adults and infants (reviewed in Aslin and Mehler (2005); Irani et al. (2007)).

NIRS for the non-invasive monitoring of brain hemodynamics was introduced more than 30 years ago by Jobsis (1977). NIRS was first applied to measure hemodynamics associated with functional brain activity in the early 1990's (Chance et al., 1993; Hoshi and Tamura, 1993; Kato et al., 1993; Vill-ringer et al., 1993). In these early days, the number of source-detector pairs (aka. channels) was limited to one or at most a few distantly placed to avoid light interference. Multichannel NIRS instruments were then developed with an array of multiple source-detector pairs that allowed simultaneous monitoring across brain regions (Maki et al., 1995). Multichannel NIRS data are often treated in a discrete manner, and subjected to channel-wise statistical analysis within a subject (e.g., Schroeter et al. (2004)) or among a group of subjects (e.g., Okamoto et al. (2006)). To form images, these multichannel NIRS data have been transformed via spatial interpolation to generate 2 dimensional topographic images of brain activation (Maki et al., 1995). Moreover, NIRS has been recently implemented with a relatively large number of densely-placed sources and detectors, allowing tomographic methods, or Diffused Optical Tomography (DOT), to reconstruct 3D images of brain activation (Bluestone et al., 2001; Ze et al., 2007; Culver et al., 2003). DOT uses short and long distance measurements to provide depth resolution and enables separation of superficial scalp signals from deeper brain signals.

DOT generally requires subject-specific spatial priors of the head anatomy for constructing 3D images of brain activation (Boas and Dale, 2005), but it is not always feasible to obtain subject-specific head anatomy. We thus propose a method to utilize a general head template (*atlas*) to construct 3D DOT images while maintaining capability of anatomical interpretation of the resultant images. This MRI-free approach to obtaining optical images is based on registering a selected atlas to the subject head surface and solving the photon migration forward problem on the registered atlas; optical measurements are acquired on the physical subject; and then a map of the cortical absorption coefficient changes is calculated.

We first describe the atlas-based DOT method, including the atlas selection criteria, the dataset, the registration algorithm, the tissue optical properties, the probe design, the photon migration simulation, and the inverse problem solution. The hemodynamic response to median nerve stimulation measured in three healthy individuals is reconstructed using the subject-specific brain anatomy as well as the atlas, and the spatial localization accuracy is estimated. The results indicate that by using an atlas as a general head model, it is possible to reconstruct the location of the activation focus within the correct gyrus.

1. Materials and methods

1.1. Atlas-guided image processing

Diffuse optical tomography comprises two steps: In the forward model ($y = Ax$), photon migration is simulated in a segmented head obtained from an anatomical MRI. This forward model produces, for source-detector pair, a spatial map of the sensitivity to absorption changes within the head. This spatial sensitivity to absorption changes for each source-detector pair is represented by a row in matrix A . The second step is the solution of the inverse problem ($\hat{x}_B = \min \|A_x - y\|^2 + \tau\|x\|^2$): the Tikhonov regularization parameter τ (Bertero and Boccacci, 1998; Arridge, 1999) and the sensitivity map A are used in the DOT inverse problem along with simulated or experimental measurements (y) to generate a three dimensional image \hat{x}_B of the absorption changes (Arridge, 1999; Custo, 2008). When an

anatomical MRI of the subject's head is not available, we propose the use of an atlas (see Figure 1C) for the photon migration forward model. The atlas is registered to the subject's head via a scalp landmark-based registration method (SLR₁₀₋₂₀) described in Section 1.1.1. Given the optode positions, the photon migration process is simulated on the registered atlas using Monte Carlo simulations (Boas et al., 2002), resulting in a volumetric absorption sensitivity map (A). Once we have obtained measurements (y) and the forward model (A) in the subject's coordinate system, we proceed by solving the inverse problem ($\hat{x}_B = \min \|A_x - y\|^2 + \tau \|x\|^2$) to obtain an image of the changes in the absorption coefficient. In more detail, we first extract a mesh of points describing the atlas' scalp surface; then, for each subject, we perform the following steps:

1. Place the optical probe on the subject (locate the brain area of interest for the desired experiment and place the set of sources and detectors centered on it), then, measure the 3D coordinates of the sources and detectors as placed on the subject head and extract a mesh of points describing the subject's scalp surface;
2. Acquire baseline (rest state) and activation (median-nerve stimulation) optical measurements on the subject;
3. Use the subject's and atlas' scalp meshes to estimate the affine registration parameters T that minimize the discrepancy between specific landmarks on the scalp meshes;
4. Apply T to map the atlas to the subject space (Figure 1A);
5. Modify the registered atlas' Cerebral Spinal Fluid (CSF) thickness using dilation/erosion to match the subject's median CSF thickness, as estimated from the subject's age according to the linear model estimated in Figure 2; according to a recent study on the sensitivity of optical measurements to CSF thickness (Custo and Wells, 2007) shows that a 50% change in CSF thickness produces small errors (less than 15% for separation less than 32 mm from the source);
6. Project the probe, as measured on the subject (see Figure 3), onto the registered atlas (Figure 1B);
7. Simulate photon migration on the registered atlas using a Monte Carlo algorithm (Boas et al., 2002) and the atlas optical properties (see Table 1);
8. For validation purposes, simulate photon migration on the subject head using its four tissue types segmentation and optical properties (see Table 1);
9. Solve the DOT inverse problem to reconstruct the vascular response to brain activity (see Section 1.1.3). The image is thus obtained using an atlas head instead of the subject-specific head.

1.1.1. Registration (SLR₁₀₋₂₀)—We need to register the atlas head geometry to the subject's head based solely on external features. We developed a registration algorithm, the Scalp Landmark Registration (SLR₁₀₋₂₀) based on the alignment of scalp landmarks known as the EEG 10-20 electrode system (Jasper, 1958). The 10-20 system is a collection of anatomically specified points on the scalp. The location of the *nasion* (bridge of the nose), the ear canals, and the *incave* on the back of the skull provide cues to define the Nz, A1, A2, and Iz points, respectively. The remaining 10-20 points are calculated with respect to the relative distances between these four points along the scalp surface lines connecting them (Jasper, 1958).

We begin the registration by manually extracting the four initial anchor points, Nz, Iz, A1 and A2, from the atlas and the subject surface meshes. The surface mesh can be extracted

from an MRI or, when the physical subject is available, the subject's four anchor point locations can be acquired using a commercially available 3D digitizer. Using the four initial points we proceeded by calculating the locations of the other 10-20 points on the subject and the atlas using the Jurcak et al. virtual 10-20 algorithm (Jurcak et al., 2005, 2007); this step also can be performed on the subject using a 3D digitizer instead of the subject scalp mesh extracted from the anatomical MRI. From the set of 10-20 points on the subject (P_{sbj}) and the atlas (P_{mni}), given that $P_{mni} = T * P_{sbj}$, we estimate the 3×4 affine transformation T as the least squares solution of the overdetermined linear system (Singh et al., 2005).

Analogous registration algorithms are described in (Darvas et al., 2006) and (Fuchs et al., 2002).

1.1.2. Diffuse Optical Tomography forward solution—We used a Monte Carlo solution of the Radiative Transport Equation (RTE) to simulate photon migration in highly scattering tissues (Boas et al., 2002). Alternatively, it is possible to use faster but less accurate methods based on Diffusion Approximation (for example, less than 28.4% error in time-domain partial path-length prediction using Finite difference algorithm, as reported in Custo and Boas (2004)). Monte Carlo method models photon trajectories through heterogeneous tissues, reproducing the randomness of each scattering event in a stochastic fashion, and histograms the spatial distribution of the photon trajectories to estimate the Green's function of the photon fluence. We launch photons from each source to estimate the Green's function from the source position r_s to each position r_j within the head. We also launch photons from each detector position r_d to estimate the Green's function from each position in the head to the detector. To estimate each Green's function, we simulate three hundred million photons from each source/detector location. The optical properties used for the scalp, skull, CSF, and brain are indicated in Table 1 (Boas et al., 2003; Steinbrink et al., 2001; Strangman et al., 2003). A wide variation of these optical properties has been reported, however the effect of this variation on the measurements is small and negligible compared to other factors (e.g. probe placement and geometry), as shown in Strangman et al. (2003) (small changes of the optical properties due to the wavelength choice result in $\sim 10\%$ changes in the measured differential pathlength factor).

When the probability of scattering is much greater than the probability of absorption, then photon migration is well described by the diffusion equation which depends on the reduced scattering coefficient $\mu'_s = \mu'_s(1-g)$ which lumps together the scattering coefficient and the scattering anisotropy g . The value of g does not change the result in the diffusion equation provided that the value of μ'_s does not change. The Monte Carlo simulation is more efficient for smaller values of g (we use $g = 0.01$). We thus decrease the value of μ_s to obtain a value of μ'_s that is consistent with literature estimates of μ'_s in the human head.

We use a refractive index 1 for all tissues, with a negligible effect on spatial accuracy of our images in the cortex, particularly since we are reconstructing differential images. Further, the Monte Carlo simulation is faster when we neglect reflections that arise from a mis-match in the index of refraction.

Given the Green's functions, we calculate each element of the A matrix as

$$A_{m,j} = \frac{G(r_{s,m}, r_j) G(r_j, r_{d,m})}{G(r_{s,m}, r_{d,m})}, \quad (1)$$

where m is the index of the source-detector pair, j is the voxel index, and $r_{s/d,m}$ is the source/detector location for the source-detector pair m . More details are provided in (Boas et al., 2002).

1.1.3. Diffuse Optical Tomography inverse solution—Given the forward solution for the registered atlas head, we obtain the solution of the regularized inverse problem by

$$\hat{x}_B = \min \|Bx - y\|^2 + \tau \|x\|^2, \quad (2)$$

where B is the sensitivity matrix constrained to the brain, i.e.

$$B_{m,j} = \begin{cases} A_{m,j} & \text{when voxel } j \text{ is labeled gray or white matter} \\ 0 & \text{otherwise} \end{cases}, \quad (3)$$

τ is the scalar Tikhonov regularization parameter (Bertero and Boccacci, 1998; Arridge, 1999) and $\tau = \alpha \cdot \max_i (\sum_k B_{i,k})^2$ and typically $\alpha = 0.01$ (Boas and Dale, 2005); y is the detected optical signal normalized by the baseline optical signal for each source-detector pair; and x is the image of the absorption changes associated with the brain activation. We obtain the solution for \hat{x}_B by (Arridge, 1999; Boas and Dale, 2005):

$$\hat{x}_B = B^T (BB^T + \tau I)^{-1} y,$$

where I is the identity matrix (Boas and Dale, 2005).

For validation purposes, we also solve \hat{x}_B for B_{sbj} , that is, the sensitivity matrix calculated using the brain voxels of the subject specific anatomy to guide the photon migration forward model.

1.2. Head Atlas

When the subject specific anatomy is not available, the head atlas serves as a substitute. As the photon migration process is simulated on the optical model derived from the atlas, it is important to have an accurate segmentation of the chosen atlas with a spatial resolution on the order of 1 mm. We chose the well documented MNI single subject atlas (Collins et al., 1998): this model is constructed from a high-resolution (1 mm isotropic voxels) low-noise dataset that was created by registering and averaging 27 scans (T1-weighted gradient echo acquisitions with TR/TE/FA = 18 ms/10 ms/30 deg) of the same individual in stereotactic space (Holmes et al., 1998). The volume contains $181 \times 217 \times 181$ voxels and covers the head completely, extending from the top of the scalp to the base of the foramen magnum. A five tissue labeled model was derived from the nine tissue types model available from BrainWeb (BrainWeb, URL; Collins et al., 1998) by relabeling connective tissue, fat, muscle/skin as skin, and glial matter as white matter (brain). The resulting discrete model is a volume of $181 \times 217 \times 181 \text{ mm}^3$ voxels. We used the following principles to select and customize the atlas:

1. We selected an atlas with an accurate segmentation. We have shown how critical an accurate labeling of the Cerebral Spinal Fluid (CSF) is for the forward model (Custo and Wells, 2007), and although we significantly improved CSF segmentation with our semi-supervised segmentor (see Custo et al. (2008)), the ambiguity of the typical CSF T1-weighted MR intensity values made it difficult to achieve an accurate segmentation of the CSF. The most effective way to separate

CSF from gray matter and skin-like tissues (such as muscle, fat, bone marrow, skin, dura) is to combine anatomical data from various sources (such as manual labeling of T1- and T2-weighted MR scans, and proton density data) as is done for the MNI single subject atlas (Collins et al., 1998).

2. Selecting a standard and well-documented atlas is advantageous, as expressing measurements in this standard MNI space makes it easier to compare results with others, and provides a familiar framework in which to present results.
3. Given an atlas, we want to minimize the difference with respect to individual subjects. We achieve this by adjusting the atlas CSF median thickness based on the subject's age. We have estimated from the anatomical MRI's of 32 healthy subjects, ranging in age from 21 to 77 years, the median CSF thickness across the sampled head voxels, and showed that it roughly increases linearly with age (Custo et al., 2008; Custo, 2008) (see the median CSF thickness plot of Figure 2). Thus, given the subject's age, we either dilate or erode the registered atlas CSF to match the expected subject median CSF thickness, reducing or increasing the cortical thickness respectively.

1.3. Experimental Optical Measurements of Brain Activation

For this study, we recorded optical measurements during somatosensory cortical stimulation in humans. Diffuse optical tomography was performed using a continuous-wave system (CW4, TechEn Inc.), with 8 source-positions (2 wavelengths each, 690 and 830 nm) and 8 detectors in an array of 2 columns of light sources interleaved with 2 columns of light detectors. After acquisition, data was down sampled to 10 Hz, band-pass filtered between 0.01 and 0.5 Hz, and the optical intensity was converted to chromophore concentration changes using the modified Beer-Lambert law. Anatomical MRI scans were also obtained using a T1-weighted MPRAGE sequence ($1 \times 1 \times 1$ mm resolution, $TR/TE/\alpha = 2.53$ s/1.64 ms/7°) (Mesquita et al., 2008).

The stimulation protocol consisted of an event-related median-nerve stimulation, at motor threshold for the right thumb, in 3 healthy right-handed subjects (25, 34, and 31 years old). The stimulus was presented at 3 Hz for a 4 sec duration. A total of 50 trials of this stimulus were acquired for each subject (Mesquita et al., 2008).

For validation purposes, the forward model is solved on each subject's head as well as on the atlas registered to each subject, and the images reconstructed when using the subject sensitivity map (A_{sbj}) versus the registered atlas (A_{atl}) are compared. With this goal in mind, each subject's anatomical MRI is segmented into skin-skull-CSF-brain using FreeSurfer's `mri_watershed` automatic segmentation tool (FreeSurfer, URL; Ségonne et al., 2004). This initial estimate is refined into a more accurate CSF segmentation by labeling as CSF only those voxels labeled CSF by `mri_watershed` and that are within the intensity range of the CSF. Then, the remainder of the voxels formerly labeled as CSF by `mri_watershed` are relabeled as skull. These are voxels outside the CSF intensity range but surrounding CSF, that constitute our best definition of skull voxels. A more detailed description of the segmentation method can be found in Custo et al. (2008).

We used the MNI single subject atlas as our general anatomical model and we created a database of 3 atlases registered to each of the 3 subjects with our SLR_{10-20} algorithm and with a modified CSF thickness to match that of the subject to which they are registered, using the age model described in Figure 2.

The optical probe is designed to cover the left hemisphere motor and pre-motor cortices. The probe comprises eight sources (red) and eight detectors (white) in a 4×4 grid. Each detector/

source is set 2 cm apart from the closest detector/source and 3 cm apart from the closest source/detector, as shown in Figure 3. We extracted the approximate locations of the physical optodes from the anatomical MR scan using vitamin E markers and then projected these locations onto the surface of the head toward the anterior commissure point (the locations of the eight sources are shown in red, and the eight detectors are shown in white). We then proceeded similarly for the registered atlases, starting with the same approximated locations of the optodes visible on the subjects' MR scans and then projecting them onto the registered atlases' scalp surfaces.

2. Results

The brain activation images reconstructed in the subject and registered atlas heads are shown in Figures 4, 5 and 6. Figure 4 shows a visual representation of the results for subject c (the same as in Figure 5c). The subject (left image) and corresponding registered atlas (right image) activation maps are plotted on the cortical surfaces and the probe location is also shown. The activation contrast has been thresholded at half maximum, for better visualization and to focus the comparison between subject- and atlas-based reconstructions ($RECON_s$ and $RECON_a$, respectively) on the spatial localization rather than on the signal amplitude.

Figure 5a-c shows the brain activity images for three experimental subjects and their corresponding registered atlases. One will readily notice that the reconstructed images using subject-specific ($RECON_s$) or atlas anatomy ($RECON_a$) are localized in the same gyri: for the subjects described in Figure 5a and 5c the activation peaks are in the post-central gyrus (ventral and dorsal sections, respectively), where the primary somatosensory areas lie (mainly BA1, BA2, and BA3b), as expected from a typical median-nerve stimulus (Korvenoja et al., 2006; Ferretti et al., 2007; Arienzo et al., 2006). In contrast, in the subject analyzed in Figure 5b the activation focus is found in the posterior bank of the post-central gyrus (partially corresponding to the secondary somatosensory area, or SII) in both $RECON_s$ and $RECON_a$. The lack of source-detector pairs probing more frontal regions is the likely explanation for not observing a vascular response in the primary somatosensory area.

Figure 6 shows the reconstructed brain activation in subject c using FreeSurfer surface representation tools (FreeSurfer, URL; Fischl et al., 1999a; Dale et al., 1999; Fischl et al., 2001). The bottom row shows the overlap (yellow) of $RECON_a$ (blue) and $RECON_s$ (red) reconstructed active areas when the vascular response from $RECON_a$ has been registered to the subject cortical surface using the anatomically-guided registration algorithm described in Fischl et al. (1999b). Activation is reconstructed in the same section of the same gyrus (dorsal section of the post-central gyrus), responsible for the primary somatosensory functions, independently of the choice of head model. The high level of agreement between $RECON_s$ and $RECON_a$ is clearly shown by the large overlap region (in yellow), suggesting that an accurate prediction of active cortical foci can be obtained using an atlas-based head model.

In Table 2 we compare the areas of activation that were estimated using subject-specific ($RECON_s$) and atlas-based ($RECON_a$) methods for the 3 subjects. The "overlap" column indicates the fraction of the activating voxels estimated by one method that were in agreement with the other method. In addition, the size of the activation regions, as well as the Dice measure of agreement of the predicted activating regions, are reported for each subject. The Dice measure has value zero if the regions are disjoint, and one if they agree completely (van Rijsbergen, 1979).

3. Conclusions

In this paper we introduced an imaging protocol that uses Diffuse Optical Tomography (DOT) to reconstruct brain activation images without the need of the subject's anatomical MRI. The approach consists of using an atlas-based anatomical model instead of the subject's anatomy and solving the photon migration forward model on the atlas model, while acquiring optical measurements from the subject, and then reconstructing the cortical activation in the registered atlas. Although subject's and atlas' anatomies do vary, the DOT images reconstructed on both templates can resolve the cortical activation at the gyrus level. The benefits of this novel method derive from eliminating the need for MRI and its associated issues such as high costs, possible subject discomfort and claustrophobia during the MR anatomical scan, limited potential for studies on neonatal subjects, and lack of portability.

We solved the DOT forward and inverse problems on three experimental subjects: optical measurements were acquired on the physical subjects and photon migration was simulated on both the subjects' heads and the atlases registered to the experimental subjects using SLR₁₀₋₂₀. The inverse problem was solved using each subject's anatomical data, and the reconstructed activation map was compared to that using the registered atlas. The qualitative results (see Figure 5) showed that the activation focus is localized in the correct gyri using the atlas model, although the subject and atlas cortical geometry was not exactly the same and the magnitude of activation was different. Overall, we showed that it is possible to use a general anatomical head model to represent the subject's head to guide the DOT forward problem and, therefore, to localize the macroanatomical structure where activation occurs. The activation reconstruction accuracy of atlas-based DOT is limited to the localization of the activation focus with macroanatomical structure spatial precision (sulci/gyri); therefore, our purely optical imaging protocol is not suitable when a higher spatial resolution is desired or when a suitable atlas to represent the specific subject is not available (for example, in patients with brain lesions in unknown locations or of unknown size). We have demonstrated the technique of atlas based Diffuse optical tomography and its potential accuracy, and motivates future validation studies of the quantitative accuracy of atlas-based reconstructions for different brain regions.

We expect results to improve further more when employing a finer spacing of source-detectors as suggested in Ze et al. (2007) and using time resolved technology, as both will contribute to increase the optical measurement spatial resolution and hence will improve the localization of brain activity. As the gyra/sulci configuration varies across subjects, the localization of the brain activity focus will be affected; we are conducting a population study to quantify this dependency and the results will appear in a future publication.

Acknowledgments

This work was supported by NIH U54-EB-005149, NIH P41-RR14075, and NIH P41-RR13218.

References

- Arienzo D, Babiloni C, Ferretti A, Caulo M, Del Gratta C, Tartaro A, Rossini P, Romani G. Somatotopy of anterior cingulate cortex (acc) and supplementary motor area (sma) for electric stimulation of the median and tibial nerves: an fmri study. *NeuroImage* 2006;33(2):700–5. [PubMed: 16935009]
- Arridge S. Optical tomography in medical imaging. *Inverse Problems* 1999;15(2):41–93. topical review.
- Aslin R, Mehler J. Near-infrared spectroscopy for functional studies of brain activity in human infants: promise, prospects, and challenges. *J Biomed Opt* 2005;10(1):11009. [PubMed: 15847575]

- Bertero, M.; Boccacci, P. Introduction to Inverse Problems in Imaging. 1998. IOP Publishing
- Bluestone AY, Abdoulaev G, Schmitz CH, Barbour RL, Hielscher AH. Three-dimensional optical tomography of hemodynamics in the human head. *Opt. Express* 2001;9(6):272–286. [PubMed: 19421298]
- Boas D, Culver J, Stott J, Dunn A. Three dimensional monte carlo code for photon migration through complex heterogeneous media including the adult human head. *Optics Express* 2002;10(3):159–170. [PubMed: 19424345]
- Boas D, Dale AM. Simulation study of magnetic resonance imaging-guided cortically constrained diffuse optical tomography of human brain function. *Applied Optics* 2005;44(10):1957–1968. [PubMed: 15813532]
- Boas D, Strangman G, Culver J, Hoge R, Jaszewski G, Poldrack R, Rosen B, Mandeville J. Can the cerebral metabolic rate of oxygen be estimated with near-infrared spectroscopy? *Physics in Medicine and Biology* 2003;48(15):2405–18. [PubMed: 12953906]
- BrainWeb. URL. <http://www.bic.mni.mcgill.ca/brainweb>
- Chance B, Zhuang Z, Unah C, Alter C, Lipton L. Cognition-activated low-frequency modulation of light absorption in human brain. *Proc Natl Acad Sci U S A* 1993;90:3770–3774. [PubMed: 8475128]
- Collins DL, Zijdenbos AP, Kollokian V, Sled J, Kabani N, Holmes C, Evans A. Design and construction of a realistic digital brain phantom. *IEEE transactions on medical imaging* 1998;17(3)
- Culver J, Siegel A, Stott J, Boas D. Volumetric diffuse optical tomography of brain activity. *Opt Lett* 2003;28(21):2061–2063. [PubMed: 14587815]
- Custo, A. Ph.D. thesis. Massachusetts Institute of Technology; Cambridge: 2008. Purely optical tomography: Atlas-based reconstruction of brain activation..
- Custo, A.; Boas, DA. OSA Technical Digest. Biomedical Optics, Optical Society of America; Miami, FL, USA: Apr. 2004 Comparison of diffusion and transport in human head..
- Custo, A.; Wells, WMI. Organization for Human Brain Mapping. Organization for Human Brain Mapping; Chicago, IL, USA: Jun. 2007 Effect of csf thickness in diffuse optical imaging..
- Custo, A.; Wells, WMI.; Grimson, W. Organization for Human Brain Mapping. Organization for Human Brain Mapping; Melbourne, Australia: Jun. 2008 Age and gender effect on cerebral spinal fluid thickness..
- Dale A, Fischl B, Sereno M. Cortical surface-based analysis i: Segmentation and surface reconstruction. *NeuroImage* 1999;9(2):179–194. [PubMed: 9931268]
- Darvas F, Ermer JJ, Mosher JC, Leahy RM. Generic head models for atlas-based eeg source analysis. *Human Brain Mapping* 2006;27:129–143. [PubMed: 16037984]
- Ferretti A, Babiloni C, Arienzo D, Del Gratta C, Rossini P, Tartaro A, Romani G. Cortical brain responses during passive nonpainful median nerve stimulation at low frequencies (0.5–4 hz): an fmri study. *Hum Brain Mapp* 2007;28(7):645–53. [PubMed: 17094120]
- Fischl B, Liu A, Dale A. Automated manifold surgery: Constructing geometrically accurate and topologically correct models of the human cerebral cortex. *IEEE Transactions on Medical Imaging* 2001;20(1):70–80. [PubMed: 11293693]
- Fischl B, Sereno M, Dale AM. Cortical surface-based analysis ii: Inflation, flattening and surface-based coordinate system. *NeuroImage* 1999a;9:195–207. [PubMed: 9931269]
- Fischl B, Sereno M, Tootell R, Dale A. High-resolution inter-subject averaging and a coordinate system for the cortical surface. *Human Brain Mapping* 1999b;8:272–284. [PubMed: 10619420]
- FreeSurfer. URL. <https://surfer.nmr.mgh.harvard.edu/fswiki>
- Fuchs M, Kastner J, Wagner M, Hawes S, Ebersole J. A standardized boundary element method volume conductor model. *Clin Neurophysiol* 2002;113(5):702–712. [PubMed: 11976050]
- Holmes C, Hoge R, Collins DL, Woods R, Toga A, Evans A. Enhancement of mr images using registration for signal averaging. *Journal of Computer Assisted Tomography* 1998;22:324–333. [PubMed: 9530404]
- Hoshi Y, Tamura M. Dynamic multichannel near-infrared optical imaging of human brain activity. *J Appl Physiol* 1993;75:1842–1846. [PubMed: 8282640]

- Irani F, Platek S, Bunce S, Ruocco A, Chute D. Functional near infrared spectroscopy (fnirs): an emerging neuroimaging technology with important applications for the study of brain disorders. *Clin Neuropsychol* 2007;21(1):9–37. review. [PubMed: 17366276]
- Jasper H. The ten-twenty electrode system of the international federation. *Electroencephalogr Clin Neurophysiol* 1958;10:371–375.
- Jobsis F. Noninvasive, infrared monitoring of cerebral and myocardial oxygen sufficiency and circulatory parameters. *Science* 1977;198:1264–1267. [PubMed: 929199]
- Jurcak V, Okamoto M, Singh A, Dan I. Virtual 10-20 measurement on mr images for inter-modal linking of transcranial and tomographic neuroimaging methods. *NeuroImage* 2005;26:1184–1192. [PubMed: 15961052]
- Jurcak V, Tsuzuki D, Dan I. 10/20, 10/10 and 10/5 systems revisited: their validity as relative head-surface-based positioning systems. *NeuroImage* 2007;34(4):1600–1611. [PubMed: 17207640]
- Kato T, Kamei A, Takashima S, Ozaki T. Human visual cortical function during photic stimulation monitoring by means of near-infrared spectroscopy. *J Cereb Blood Flow Metab* 1993;13:516–520. [PubMed: 8478409]
- Korvenoja A, Kirveskari E, Aronen H, Avikainen S, Brander A, Huttunen J, Ilmoniemi R, Jääskeläinen J, Kovala T, Mäkelä J, Salli E, Seppä M. Sensorimotor cortex localization: comparison of magnetoencephalography, functional mr imaging, and intraoperative cortical mapping. *Radiology* 2006;241(1):213–22. [PubMed: 16908676]
- Maki A, Yamashita Y, Ito Y, Watanabe E, Mayanagi Y, Koizumi H. Spatial and temporal analysis of human motor activity using noninvasive nir topography. *Med Phys* 1995;22:1997–2005. [PubMed: 8746704]
- Mesquita, R.; Radhakrishnan, H.; Mandeville, J.; Huppert, T.; Franceschini, M.; Covolan, R.; Boas, D. Organization for Human Brain Mapping. Organization for Human Brain Mapping; Melbourne, Australia: Jun. 2008 Imaging oxygen consumption with near-infrared spectroscopy and fmri simultaneously..
- Obrig H, Villringer A. Non-invasive neuroimaging using near-infrared light. *Journal of Cerebral Blood Flow and Metabolism* 2003;23:1–18. [PubMed: 12500086]
- Okamoto M, Matsunami M, Dan H, Kohata T, Kohyama K, Dan I. Prefrontal activity during taste encoding: an fnirs study. *Neuroimage* 2006;31(2):796–806. [PubMed: 16473020]
- Ségonne F, Dale A, Busa E, Glessner M, Salat D, Hahn H, Fischl B. A hybrid approach to the skull stripping problem in mri. *NeuroImage* 2004;22(3):1060–1075. [PubMed: 15219578]
- Schroeter M, Bücheler M, Müller K, Uludağ K, Obrig H, Lohmann G, Tittgemeyer M, Villringer A, von Cramon D. Towards a standard analysis for functional near-infrared imaging. *Neuroimage* 2004;21(1):283–90. [PubMed: 14741666]
- Shibasaki H. Human brain mapping: hemodynamic response and electrophysiology. *Clin Neurophysiol* 2008;119(4):731–43. review. [PubMed: 18187361]
- Singh A, Okamoto M, Dan H, Jurcak V, Dan I. Spatial registration of multichannel multi-subject fnirs data to mni space without mri. *NeuroImage* 2005;27(4):842–851. [PubMed: 15979346]
- Steinbrink J, Wabnitz H, Obrig H, Villringer A, Rinneberg H. Determining changes in nir absorption using a layered model of the human head. *Phys Med Biol* 2001;46(3):879–896. [PubMed: 11277232]
- Strangman G, Boas D, Sutton J. Non-invasive neuroimaging using near-infrared light. *Biological Psychiatry* 2002;52:679–693. [PubMed: 12372658]
- Strangman G, Franceschini MA, Boas DA. Factors affecting the accuracy of near-infrared spectroscopy concentration calculations for focal changes in oxygenation parameters. *Neuroimage* 2003;18:865–879. [PubMed: 12725763]
- Toronov V, Zhang X, Webb A. A spatial and temporal comparison of hemodynamic signals measured using optical and functional magnetic resonance imaging during activation in the human primary visual cortex. *NeuroImage* 2007;34(3):1136–1148. [PubMed: 17134913]
- van Rijsbergen, C. Information Retrieval. Butterworths; London: 1979.
- Villringer A, Planck J, Hock C, Schleinkofer L, Dirnagl U. Near infrared spectroscopy (nirs): a new tool to study hemodynamic changes during activation of brain function in human adults. *Neurosci Lett* 1993;154:101–104. [PubMed: 8361619]

Zeff B, White B, Deghani H, Schlaggar B, Culver J. Retinotopic mapping of adult human visual cortex with high-density diffuse optical tomography. *Proc Natl Acad Sci U S A* 2007;104(29):12169–74. [PubMed: 17616584]

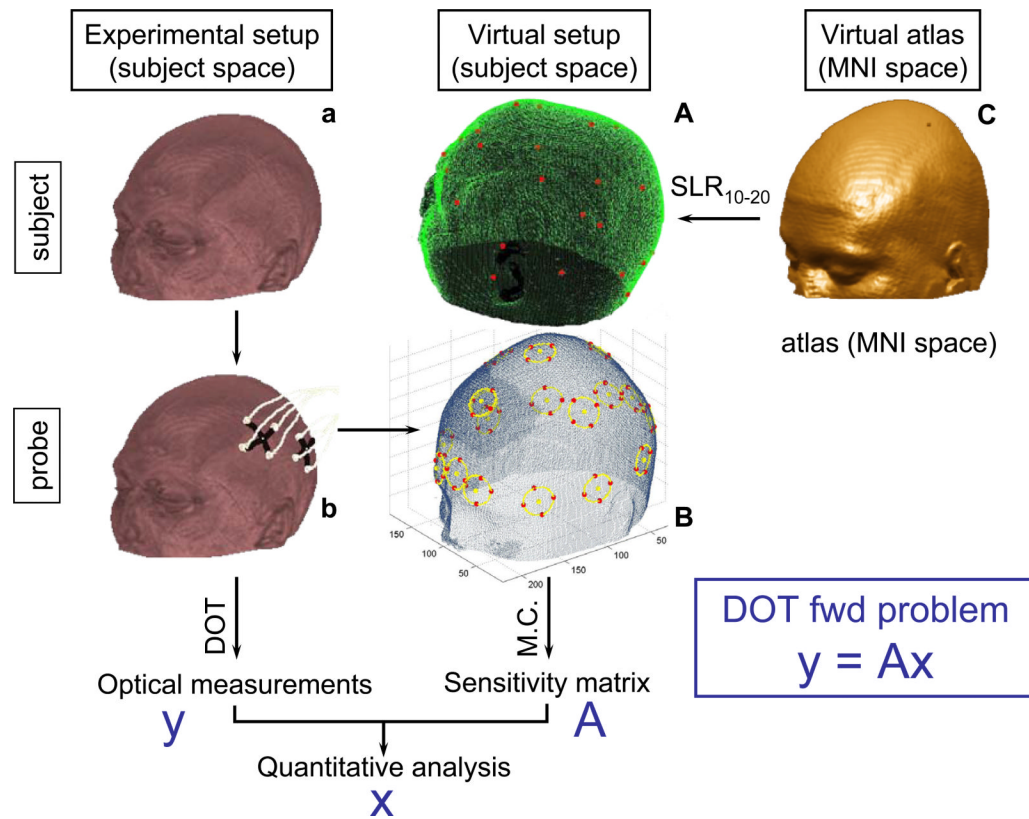


Figure 1.

On the subject's head (a) we place the physical probe (b) and acquire optical measurements. We register the MNI atlas (C) to the subject's scalp using SLR_{10-20} (A) and then project the locations of the probe onto the registered atlas scalp (B). Having defined the virtual probe on the registered atlas, we simulate photon migration on the registered atlas using a Monte Carlo algorithm, producing the sensitivity matrix which, combined with the optical measurements, forms the input of the DOT inverse problem.

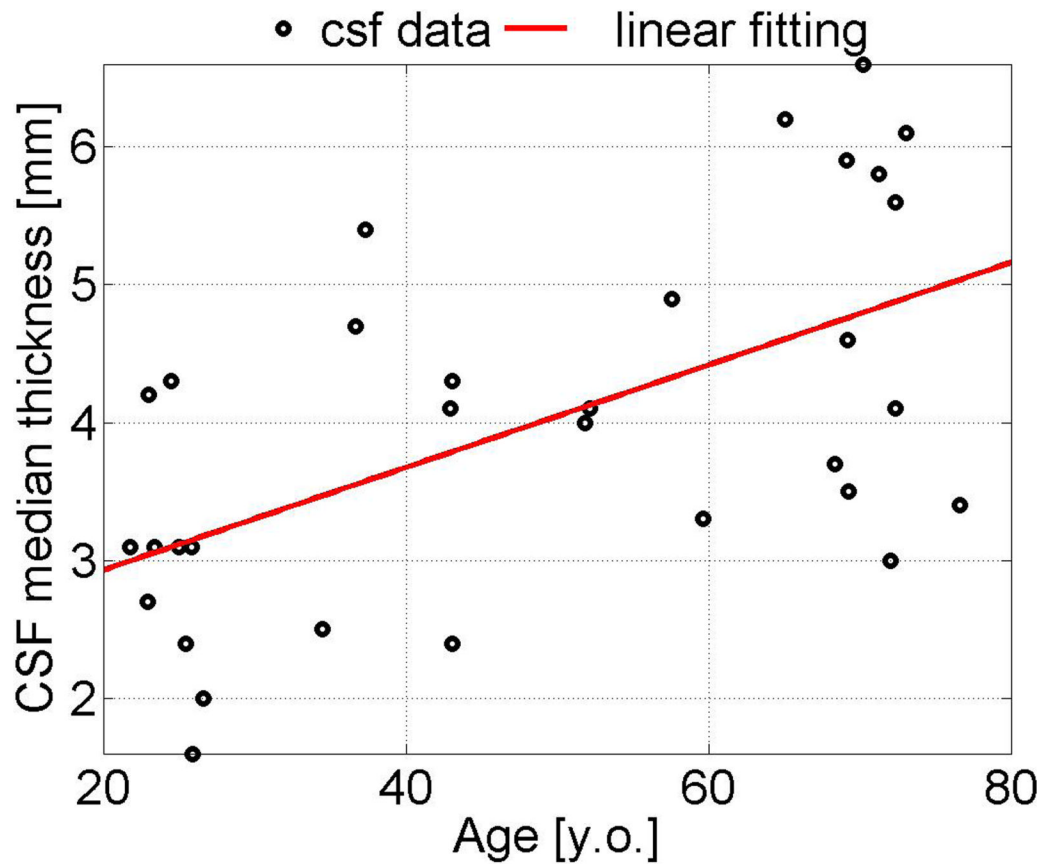


Figure 2. Linear fitting of the data points from the CSF-age study of Custo et al. (2008) (correlation coefficient 0.57 with significance $p \ll 0.005$): the black circles represent the CSF thickness median over the sampled scalp points. To customize the atlas to the target subject, we estimate the subject's median CSF thickness given its age from this linear model. Then we dilate or erode the registered atlas' CSF layer to match the subject's estimated value.

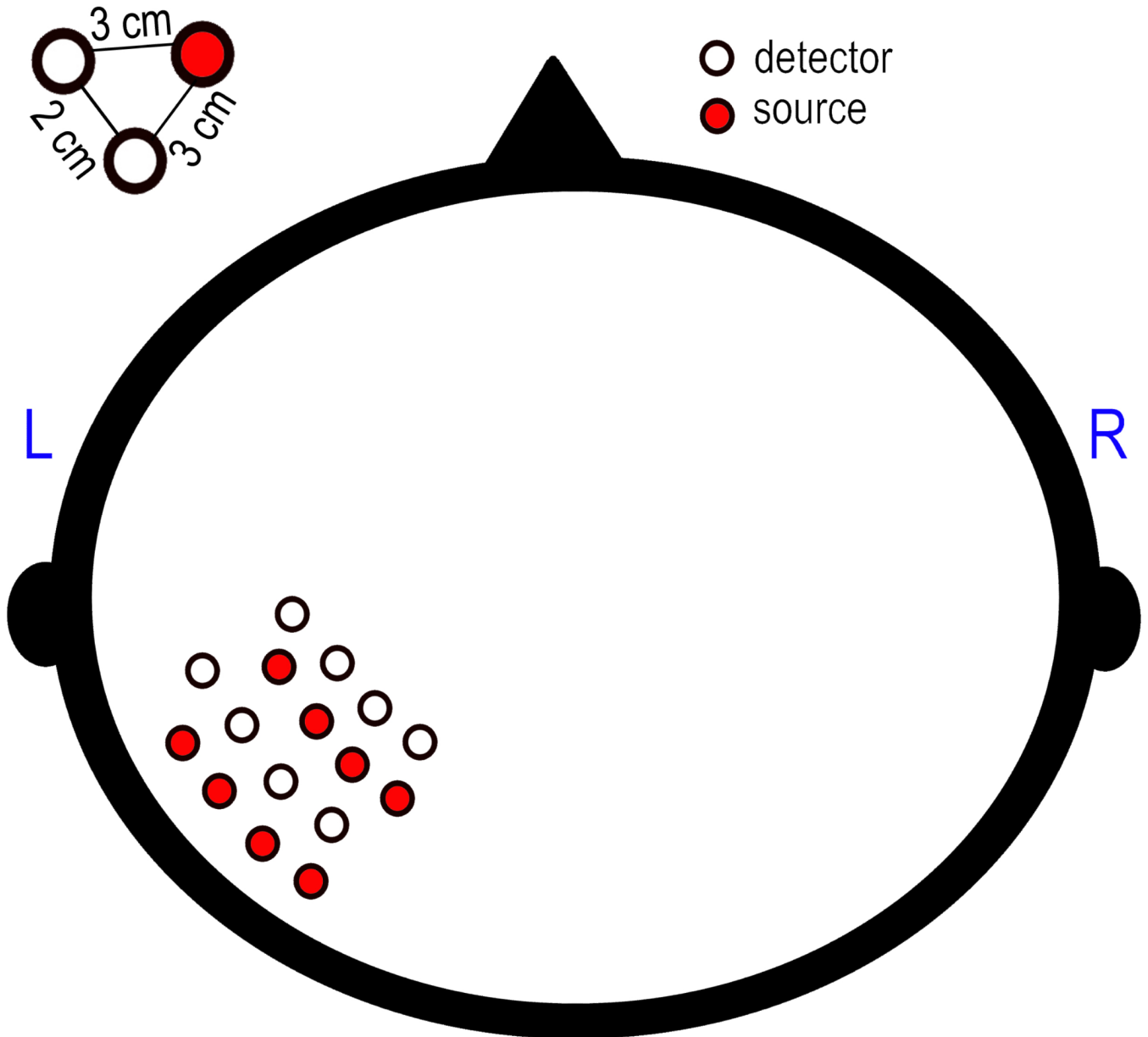


Figure 3.

The experimental probe is designed to cover the left hemisphere motor and pre-motor cortex. The probe consists of eight sources (red) and eight detectors (white) in a 4x4 grid. Each detector/source is set 2 cm apart from the closest detector/source and 3 cm apart from the closest source/detector.

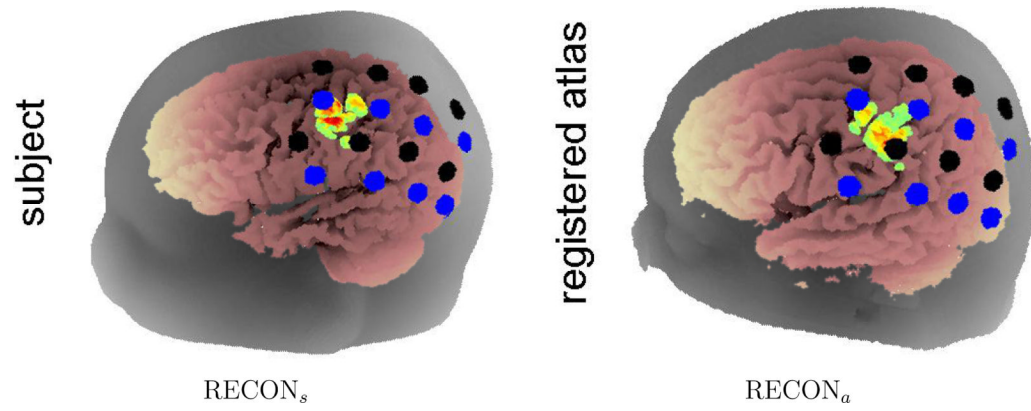


Figure 4.

Localizing activation: the subject (left) and corresponding registered atlas (right) activation maps are plotted on the cortical surfaces (pink shade) and the scalp surfaces are shaded in gray; the sources (blue circles) and detectors (black circles) locations are also shown. The activation contrast has been thresholded at half maximum (colorbar is arbitrary).

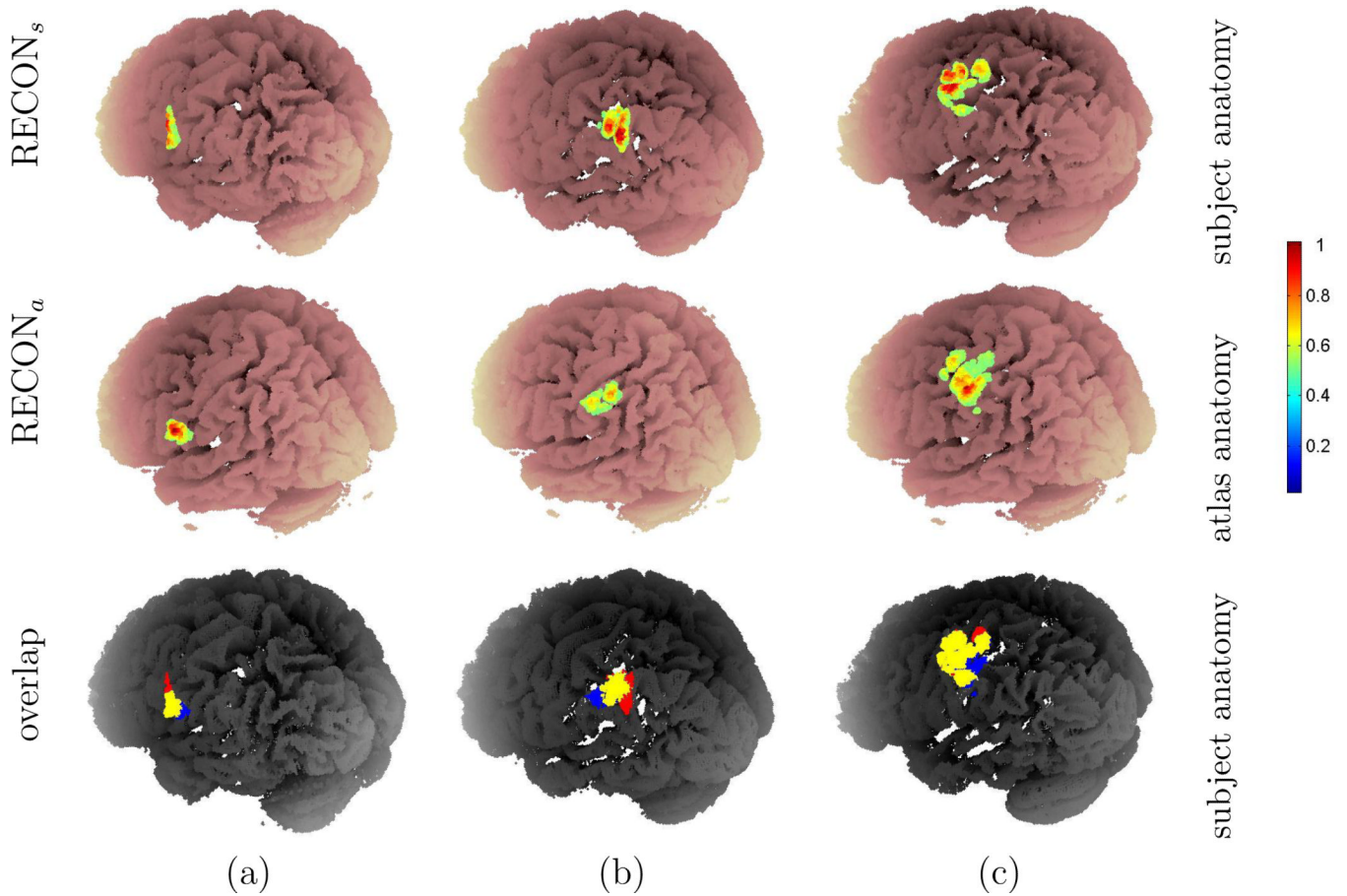


Figure 5.

Localizing vascular response to brain activation in the three experimental subjects a, b and c (one for each column); the subject- (top row, $RECON_s$, one subject per column) and corresponding registered atlas-based reconstructed activation maps (second row, $RECON_a$) are plotted on the cortical surfaces (pink shade). The bottom row shows the overlap of the top and middle rows: the blue area is the active region from the second row (atlas-based), the red area is the active region from the top row (subject-based), and the overlap of these two areas is showed in yellow. The activation contrast has been thresholded at half maximum, for better visualization and to focus the comparison between subject- and atlas-based reconstructions on the spatial localization rather than on the signal amplitude, and therefore the colorbar is arbitrary. Subject (a) and (c) show activation in the anterior bank of the ventral section (a) and dorsal section (c) of the post-central gyrus (primary somatosensory area, SI); subject (b)'s highest hemodynamic response is registered in the secondary somatosensory area (SII), in the posterior bank of the post-central gyrus due to lack of optodes probing the SI region.

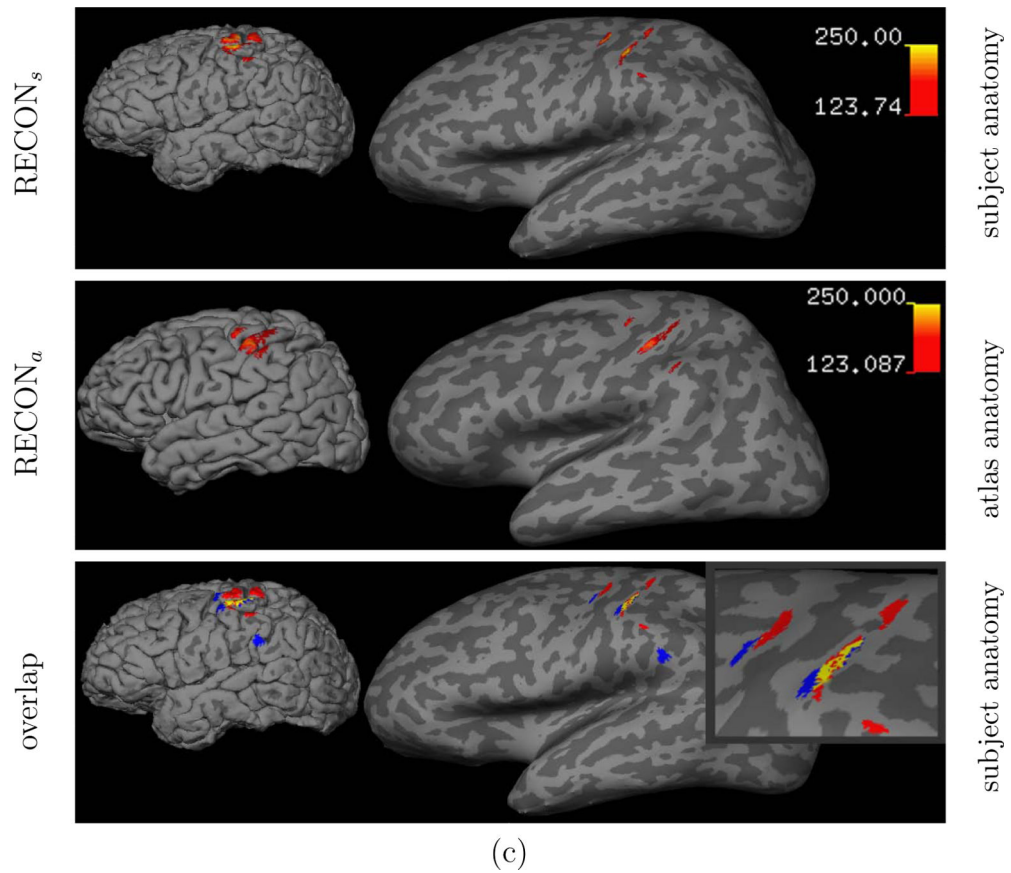


Figure 6.

Reconstructed brain activation in subject *c* using FreeSurfer surface representation tools. The top row shows the active regions in $RECON_s$ on the pial surface (left) and on the inflated cortical surface (right), the second row shows the response obtained using $RECON_a$, and the bottom row shows the overlap (yellow) of $RECON_a$ (blue) and $RECON_s$ (red) reconstructed active areas. The activation focus is on the dorsal section of the post-central gyrus (Brodmann areas 3, 1, and 2).

Table 1

Optical properties

Tissue type	μ_a [mm ⁻¹]	μ_s [mm ⁻¹]
scalp	0.0159	0.8
skull	0.0101	1.0
CSF	0.0004	0.01
brain	0.0178	1.25

Table 2

Activation overlap

subject		overlap	activation size [voxels]	Dice's coef.
a	RECON _s	88%	311	0.86
	RECON _a	84%	265	
b	RECON _s	65%	425	0.76
	RECON _a	93%	294	
c	RECON _s	70%	795	0.76
	RECON _a	83%	836	